Analysis and Comparison of Multichannel SAR Imaging Algorithms

Risto Vehmas, Juha Jylhä, Minna Väilä, and Ari Visa
Tampere University of Technology, Laboratory of Signal Processing, Tampere, Finland
Email: risto.vehmas@tut.fi

Abstract—**Multichannel synthetic aperture radar (MSAR) systems are essential for applications such as ground moving target indication (GMTI), interferometric SAR (InSAR), and high-resolution wide-swath (HRWS) imaging. In this paper, we analyze and compare MSAR image reconstruction algorithms. Previously, image reconstruction for MSAR has relied heavily on frequency domain matched filtering. Time domain image reconstruction algorithms have several attractive qualities, but their use has been limited due to a high computational burden. In this paper, we utilize digital beamforming and the phase center approximation to develop a fast time domain (fast factorized back-projection, FFBP) algorithm for MSAR. We present two FFBP implementations for MSAR and perform a comparative study between MSAR imaging algorithms. The numerical results confirm the feasibility of the proposed FFBP algorithms for MSAR.**

Index Terms—**synthetic aperture radar, radar imaging, radar signal processing, digital beamforming**

I. INTRODUCTION

The advancements in phased array radar technology and the increase in computational power further the development of multichannel synthetic aperture radar (MSAR) systems. MSAR systems are important for ground moving target indication (GMTI) [1], interferometric SAR (InSAR) [2], and high resolution wide-swath (HRWS) imaging [3]. By utilizing a multichannel system, the functionality of the radar becomes increasingly controlled by software and digital signal processing algorithms.

MSAR systems are especially important in HRWS SAR imaging [3], [4]. The demand for higher spatial resolution and larger area coverage poses contradictory requirements for conventional monostatic single-channel SAR systems. The cause of this contradiction is the fact that in the conventional stripmap imaging mode, high spatial resolution in the cross-range direction requires a long synthetic aperture, and the unambiguous sampling of the full aperture thus requires a high pulse repetition frequency (PRF). For conventional waveforms, the PRF sets a limit for the width of the unambiguous range swath. This causes a trade-off between the swath width and spatial resolution resulting in degraded performance, especially for space-borne SAR sensors.

The basic idea of the MSAR system is to amplify, down-convert, digitize, and store the signal for each receive channel separately. This allows for the use of several sophisticated techniques such as space-time adaptive processing for GMTI, along track interferometry (ATI), and digital beamforming for

HRWS imaging. In HRWS imaging, typically the objective has been to manipulate the signals of the individual receivers in such a way that conventional monostatic SAR image reconstruction algorithms can be used [4].

SAR image reconstruction algorithms come in two broad classes: fast frequency domain algorithms and exact time domain algorithms. The range-Doppler (RDA), chirp scaling (CSA) and range migration (RMA) algorithms are examples of the first class [5]–[7], while the second class is based on the convolution back-projection (BP) algorithm from computer-aided tomography [8]. The computational efficiency of the frequency domain algorithms is based on utilizing the correlation theorem and the fast Fourier transform (FFT) algorithm. The increased computational power is making time domain algorithms an attractive alternative. Compared to frequency domain algorithms, time domain algorithms have several important advantages: non-uniform spatial sampling along the synthetic aperture can directly be accommodated in the processing, the image can be directly reconstructed on a digital elevation model, and non-linear trajectories can be more easily handled in the image reconstruction process.

In this paper, we formulate the image reconstruction for MSAR in its most general form and consider the implementation of fast time domain algorithms based on that formulation. Our contribution is to introduce fast time domain algorithms for MSAR, and to perform a comparative study between them and conventional MSAR imaging algorithms. Section II presents an MSAR signal model, and Section III considers MSAR image reconstruction algorithms. Section IV presents a comparative study for the MSAR algorithms, Section V discusses the results, and Section VI draws conclusions.

II. MSAR SIGNAL MODEL

A. Signal model

We consider a multichannel system consisting of a single transmitter antenna and a linear array of N receivers spaced distance d apart. The position of receiver n is denoted as $\boldsymbol{r}_{rx,n} = \boldsymbol{d}_n + \boldsymbol{r}_{tx}$, where $\boldsymbol{d}_n = [0 \ nd \ 0]^T$, $n = \lceil -N/2 \rceil, \ldots, \lceil N/2 - 1 \rceil$, and $\boldsymbol{r}_{tx}$ is the position of the transmitter. The radar platform moves along a straight line trajectory with constant velocity of magnitude v. Thus, the position of the transmitter as a function of slow-time $t \in [-T/2, T/2]$, where T is the coherent processing interval, is $\boldsymbol{r}_{tx}(t) = \boldsymbol{r}_0 + \boldsymbol{v}t$ with $\boldsymbol{v} = [0 \ v \ 0]^T$ and $\boldsymbol{r}_0 = [x_0 \ 0 \ z_0]^T$, where x_0 and z_0 are the ground range and altitude of the radar,

respectively. The transmitter emits a series of high-bandwidth pulses as the radar platform moves along its trajectory. For each transmitted pulse, all the receivers listen to the echo, amplify, down-convert, digitize and store the signal.

The received signal of a single receiver is a superposition of scaled and delayed echoes of the ideal transmitted pulse. The scale factor of each echo is determined by the reflectivity function g of the scene and the delay (and phase) by the range traveled by the signal between the transmitter and the receiver. Using the principle of superposition, the start-stop-approximation, and assuming a reflectivity distribution g for the scene, which does not depend on frequency or the aspect angle, the signal after range compression as a function of the receiver number n, radial distance (range) r, and slow-time t is

$$ss(n, r, t) = \Pi\left(\frac{t}{T}\right) \cdot$$
$$\int_{\Theta} P_n(\boldsymbol{r}, t) g(\boldsymbol{r}) A(r - \hat{r}(\boldsymbol{r}; n, t)) e^{-i\phi(\boldsymbol{r}; n, t)} d\boldsymbol{r}. \quad (1)$$

In (1) Π is the rectangle function, $\boldsymbol{r} = [x \ y \ z]^T$ is a spatial coordinate vector, $d\boldsymbol{r} = dxdydz$ is a volume element, $\Theta \subset \mathbb{R}^3$ is the support of g, and $A : \mathbb{R} \to \mathbb{R}$ is the amplitude envelope of the range-compressed pulse. In addition, $\phi(\boldsymbol{r}; n, t) = k_c \hat{r}(\boldsymbol{r}; n, t) - 2r_0$, $r_0 = \|\boldsymbol{r}_0\|$, $\hat{r}(\boldsymbol{r}; n, t) = \|\boldsymbol{r}_{tx}(t) - \boldsymbol{r}\| + \|\boldsymbol{r}_{rx,n}(t) - \boldsymbol{r}\|$, P_n is the combined two-way radiation pattern of the nth receiver and the transmitter, and k_c is the spatial carrier frequency. In (1) various system and propagation related phenomena that affect the amplitude (and possibly the phase) of the received signal are neglected.

B. Phase center approximation

The effective phase center of the transmitter-receiver pair n is located half-way between them. These effective phase centers can be regarded as approximated monostatic sample positions [3], [4]. This phase center approximation is valid when the range error $R(d_n) = \|\boldsymbol{r}_{tx} - \boldsymbol{r}\| + \|\boldsymbol{r}_{rx,n} - \boldsymbol{r}\| - 2\|\boldsymbol{r}_n\| \ll \lambda_c$, where $d_n = nd$, $\boldsymbol{r}_n = \boldsymbol{r}_{tx} + \boldsymbol{d}_n/2 - \boldsymbol{r}$ is the vector connecting the effective phase center position and the scene position $\boldsymbol{r}$, and λ_c is the carrier wavelength. Using the law of cosines in the triangle of Fig. 1, we get the range error R produced by this approximation as a function of the distance $d_n = \|\boldsymbol{d}_n\|$ between the receiver n and the transmitter as

$$R(d_n) = r_b - 2r_n = \sqrt{r_n^2 + \left(\frac{d_n}{2}\right)^2 - r_n d_n \cos\alpha}$$
$$+ \sqrt{r_n^2 + \left(\frac{d_n}{2}\right)^2 + r_n d_n \cos\alpha} - 2r_n, \quad (2)$$

where $\cos\alpha = \boldsymbol{r}_n^T \boldsymbol{d}_n / \|\boldsymbol{r}_n\| \|\boldsymbol{d}_n\|$, and $r_n = \|\boldsymbol{r}_n\|$. A simple Taylor expansion gives (retaining terms up to fourth order in d_n)

$$R(d_n) \approx \frac{d_n^2}{4r_n}\left(1 + \sin^2\alpha\right) + \frac{d_n^4}{96r_n^3}(11 - 13\sin^2\alpha). \quad (3)$$
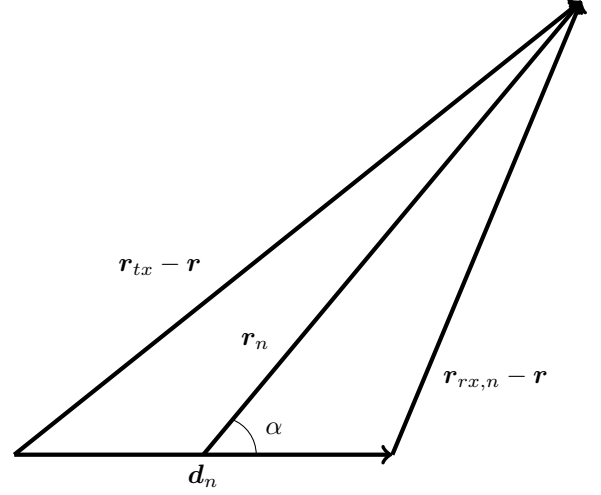

Fig. 1: The vectors used in the derivation of the error of the phase center approximation. The vector $\boldsymbol{r}_n$ connects the approximated monostatic phase center and the scene position, whereas the vector $\boldsymbol{d}_n$ connects the transmitter and the receiver.

This is clearly valid when all the receivers are on-board the same platform, since in that case we can further approximate (3) to yield the condition

$$\frac{d_n^2}{2r_n} \ll \lambda_c. \quad (4)$$

The multichannel signal (1) can thus be approximated as a monostatic single-channel signal.

Above we considered the approximation error for a fixed position $\boldsymbol{r}$ in the imaged scene. Because r_n depends on $\boldsymbol{r}$, the resulting phase error also depends on the scene position $\boldsymbol{r}$ and is thus spatially variant. In the limit where the approximation error starts to become significant (compared to λ_c), this fact has to be taken into account in addition to the requirement for d_n. In Fig. 2 we have plotted ratio between the error (3) and λ_c as a function of $\boldsymbol{r}$ by setting $z = 0$, $d_n = 1$ m and $\boldsymbol{r}_{tx} = \boldsymbol{0}$. This example depicts an airborne geometry in C-band with a 100 km^2 scene. We see that in this case the maximum error is about 0.1 percent of the carrier wavelength which results in a phase error of approximately 0.5 degrees. Clearly, the phase center approximation is accurate enough for the SAR application in question when the receiver and transmitter antennas are on-board the same platform.

C. Resolution and sampling requirements

The resolution and sampling requirements for the MSAR system can be analyzed by examining the spatial frequency content of the signal in the cross-range (y) direction. The required Fourier uncertainty relation is $\delta y = 2\pi/B_y$, where $B_y = (2k_c L)/\sqrt{r_0^2 + (L/2)^2}$ is the spatial frequency bandwidth of the signal in the slow-time direction. The length L of the synthetic aperture is determined by the half-power beamwidth θ_{hp} of the antenna pattern as $\tan\left(\theta_{hp}/2\right) = $
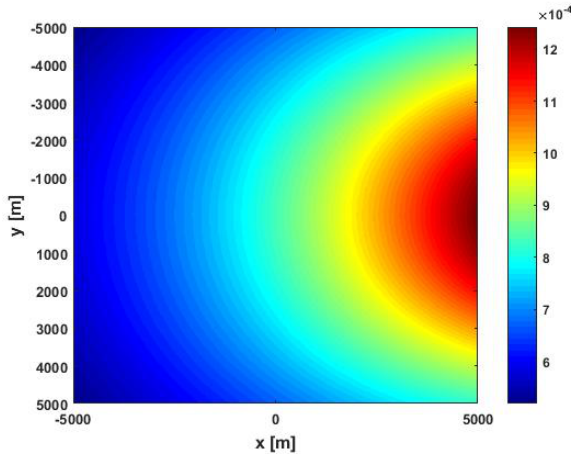
Fig. 2: The ratio between the range error of the phase center approximation and the carrier wavelength $\lambda_c = 0.06$ m when $x_0 = 8$ km and $z_0 = 6$ km. For the approximation to be valid, the ratio needs to be significantly smaller than one. The maximum phase error occurring at the position nearest to the radar on the right is about 0.5 degrees.

Fig. 3: The widths of the unambiguous range (W_r) and cross-range (L_y) swaths for a monostatic single-channel space-borne SAR system as a function of the sample spacing $\Delta y = v/f_{PR}$. A high cross-range resolution (< 1 m) will result in a narrow range swath (< 20 km).

$(L/2)/r_0$. Thus, the theoretical limit for the cross-range resolution in the stripmap operating mode is

$$\delta y = \frac{\lambda_c}{4 \sin\left(\frac{\theta_{hp}}{2}\right)}. \tag{5}$$

In the stripmap mode, the Nyquist criterion dictates that the sample spacing has to be smaller than the cross-range resolution (5). For a real single-channel system, the sample spacing in the cross-range direction is $\Delta y = v/f_{PR}$, where f_{PR} is the PRF. On the other hand, the width of the unambiguous range swath is $W_r = c/(2f_{PR})$. This causes a trade-off between swath width W_r and cross-range resolution δy, which is resolved by using a multichannel system. Fig. 3 illustrates this compromise motivating the techniques considered in the past in the context of space-borne SAR sensors operating in stripmap mode [3], [4].

We assume that all the N antenna elements have identical radiation patterns with a half-power beamwidth θ_{hp}. If we use the phase center approximation and choose $f_{PR} = 2v/Nd$, the samples in the cross-range direction are equally spaced with a sample spacing $\Delta y_n = d/2$. Thus, we can approximate the multichannel system as a monostatic single-channel stripmap system with a half-power beamwidth θ_{hp}. The difference to a real single-channel system is that now the sample spacing is determined by the element spacing d and f_{PR} (and v), whereas for a real single-channel system the sample spacing is determined by f_{PR} (and v) alone. In order to achieve the same sample spacing for a real single-channel system, the PRF would have to be N times higher than for the MSAR system in question.
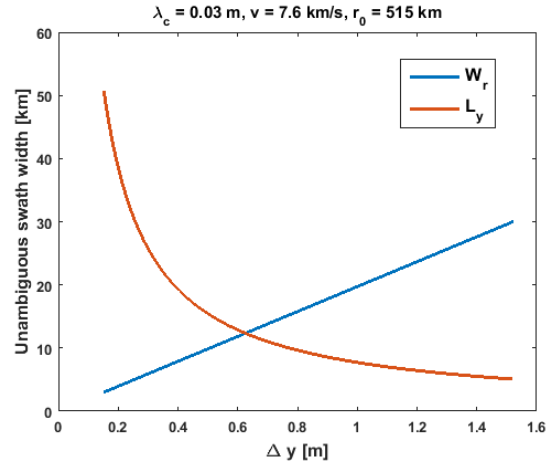
III. MSAR IMAGE RECONSTRUCTION

A. Time domain algorithms

The most general way to reconstruct an estimate for the ideal image g is to use multichannel back-projection. The image $\hat{g}$ is reconstructed using the back-projection integral

$$\hat{g}(\boldsymbol{r}) = \sum_{n=0}^{N-1} \int_{-\infty}^{\infty} ss(n, \hat{r}(\boldsymbol{r}; n, t), t) e^{i\phi(\boldsymbol{r}; n, t)} dt, \tag{6}$$

which is obtained by substituting $A(r) = \delta(r)$ for the amplitude envelope of the point target response

$$ss_{ptr}(\boldsymbol{r}; n, r, t) = A(r - \hat{r}(\boldsymbol{r}; n, t)) e^{-i\phi(\boldsymbol{r}; n, t)} \tag{7}$$

in the time domain correlation integral [9]. The integral (6) can also be expressed in the range spatial frequency k_r domain as the matched kernel correlation integral [10]

$$\hat{g}(\boldsymbol{r}) = \frac{1}{2\pi} \sum_{n=0}^{N-1} \int_{-\infty}^{\infty} \int_{-\infty}^{\infty} Ss(n, k_r, t) e^{ik_r \hat{r}(\boldsymbol{r}; n, t)} dk_r dt. \tag{8}$$

The back-projection integral (6) implies an interpolation, whereas (8) does not. However, (8) requires an additional integration over the range spatial frequencies k_r. Equations (6) and (8) represent the exact time domain image reconstruction for the multichannel signal without any approximations. The computational cost of reconstructing the image i. e. evaluating (8) for every $\boldsymbol{r}$ is proportional to $NPMM'$, when P is the number of resolution elements, M is the number of samples in the slow-time direction and M' in the range direction. Neglecting the computational cost of the interpolation, the cost of reconstructing the image using (6) is proportional to NPM.

Using the phase center approximation, we can rewrite the back-projection (6) integral as

$$\hat{g}(\boldsymbol{r}) = \int_{-\infty}^{\infty} \widetilde{ss}(2r_n(\boldsymbol{r}; y_n), y_n) e^{i\hat{\phi}(\boldsymbol{r}; y_n)} \frac{dy_n}{v}. \tag{9}$$

The notation used in (9) means defining a new integration variable y_n, which denotes the cross-range location of the approximated monostatic phase center positions. It is regarded as a continuous variable to highlight the fact that the summation of the n receiver signals for each slow-time instant t correspond to additional samples in the cross-range direction. We have also simplified the notation by making the substitution $ss(n, r, t) \rightarrow \widetilde{ss}(r, y_n)$ for the approximated monostatic range-compressed signal.

The antenna pattern of the linear receiver array can be steered to continuously illuminate an area centered at position $\boldsymbol{r}$ by applying a phase shift to each receive channel and then summing them as

$$\widehat{ss}(\boldsymbol{r}; r, t) = \sum_{n=0}^{N-1} w(n)ss(n, r, t) \exp\left[i\frac{2\pi}{\lambda_c}nd\sin\theta(\boldsymbol{r}, t)\right],$$
(10)

where w is an amplitude tapering function and the slow-time dependent angular direction θ of the beam is defined as

$$\tan\theta(\boldsymbol{r}; t) = \frac{(vt - \lceil \frac{N}{2} \rceil d) - y}{r_{min}(x, z)}.$$
(11)

In (11) the position of the first receiver is used as the reference in the beamforming and $r_{min}(x, z) = \sqrt{(x_0 - x)^2 + (z_0 - z)^2}$ is the minimum range between the radar and position $\boldsymbol{r}$. In (10) we have used a plane wave approximation, which is valid when $d_n \ll r_{min}$. Now (10) corresponds to a signal collected in spotlight mode, where the receive antenna pattern is continuously illuminating the center of the spot at $\boldsymbol{r}$. Using (10), the exact time domain image reconstruction (6) can be approximated as

$$\hat{g}(\boldsymbol{r}) = \int_{-\infty}^{\infty} \widehat{ss}(\boldsymbol{r}; 2r_{rx,0}(\boldsymbol{r}; t), t)e^{i2k_c r_{rx,0}(\boldsymbol{r};t)}dt,$$
(12)

where $r_{rx,0}(\boldsymbol{r}; t) = ||\boldsymbol{r}_{rx,0}(t) - \boldsymbol{r}||$. An efficient implementation of (12) is based on the fact that the spotlight signal $\widehat{ss}$ inside the back-projection integral is not updated for each image position $\boldsymbol{r}$. Instead, it is kept fixed for a subset of image positions (a block), whose size is determined by the size and shape of the spotlight antenna pattern and simple geometric considerations.

Without loss of generality, (12) can be written in the form

$$\hat{g}(\boldsymbol{r}) = \sum_{j=0}^{J-1} \hat{g}_j(\boldsymbol{r}),$$
(13)

where

$$\hat{g}_j(\boldsymbol{r}) = \int_{-\frac{T}{2}+j\frac{T}{J}}^{-\frac{T}{2}+(j+1)\frac{T}{J}} \widehat{ss}(\boldsymbol{r}; 2r_{rx,0}(\boldsymbol{r}; t), t)e^{i2k_c r_{rx,0}(\boldsymbol{r};t)}dt.$$
(14)

A similar partitioning of the back-projection integral into J subapertures can be done for (9). Representing the result of the integration (14) of a single subaperture j requires far less resolution elements than the final full-resolution image. This fact is utilized in the fast factorized back-projection (FFBP)

algorithm [11], [12]. First, subaperture images with coarse resolution are reconstructed on a polar grid with a large spacing in the angular direction using (14). These subaperture images are then recursively upsampled, interpolated and combined to yield the final image with full resolution.

We call the image reconstruction using (12) and FFBP the multispotlight technique. It is based on using FFBP for each block (and spotlight signal) that is formed using (10) and geometric considerations. The other FFBP implementation we use is based on using the phase center approximation in (9). It allows a straightforward implementation of the FFBP algorithm [12]; we calculate the approximated locations $\boldsymbol{r}_n$ for the additional samples, presum and downsample the resulting signal if necessary, and then reconstruct the image using the FFBP algorithm.

B. Frequency domain algorithms

Matched filtering in the frequency domain relies on the assumptions that the synthetic aperture is linear and that the approximated monostatic phase center positions are uniformly sampled. Without loss of generality, we can substitute the Fourier integrals $Ss(k_r, y_n) = \mathcal{F}_{r \rightarrow k_r}\left\{\mathcal{F}_{k_y \rightarrow y_n}^{-1}\left\{SS(k_r, k_y)\right\}\right\}$ and similarly for the point target response (7) into the time domain correlation integral, which results in (omitting unimportant constant factors of 2π)

$$\hat{g}(\boldsymbol{r}) = \int_{-\infty}^{\infty} \int_{-\infty}^{\infty} SS(k_r, k_y)SS_{ptr}^*(\boldsymbol{r}; k_r, k_y)dk_r dk_y,$$
(15)

where $SS(k_r, k_y) = \mathcal{F}_{y_n \rightarrow k_y}\left\{Ss(k_r, y_n)\right\}$ denotes the two-dimensional Fourier transform of the range-compressed signal ss. Using the Fourier shift property, (15) can be expressed as

$$\hat{g}(\boldsymbol{r}) =$$
$$\int_{-\infty}^{\infty} \int_{-\infty}^{\infty} e^{ik_y y}SS(k_r, k_y)SS_{ptr}^*([x \; 0 \; z]^T; k_r, k_y)dk_r dk_y$$
$$= \mathcal{F}_{k_y \rightarrow y}^{-1}\left\{\int_{-\infty}^{\infty} SS(k_r, k_y)SS_{ptr}^*([x \; 0 \; z]^T; k_r, k_y)dk_r\right\}.$$
(16)

The importance of (16) is that only one integration kernel SS_{ptr} is needed for every x-coordinate, and the inverse Fourier transform in (16) produces a single x-slice of the image. Image reconstruction via (16) is called either the range stacking (RSA) or wavefront reconstruction algorithm [9].

The fact that the image reconstruction (16) requires a two-dimensional correlation with a different kernel SS_{ptr} for each x-position results in a high computational burden. For this reason, several different SAR image reconstruction algorithms have been developed in the past to reconstruct the SAR image in a computationally feasible manner. For the linear synthetic aperture, the reconstruction equation (16) can be further simplified by deriving analytic expressions for the Fourier transforms sS_{ptr} and SS_{ptr}. This results in the range-Doppler (RDA) [5], [13] and range migration algorithms (RMA, also called the ω - k and the wavenumber domain algorithm) [7], [14], [15], respectively. The Fourier transforms cannot

TABLE I: Simulation parameters

Parameter	Value (simulation # 1)	Value (simulation # 2)
x_0	10 km	10 km
z_0	0 km	10 km
L	1 km	2 km
λ_c	0.10 m	0.03 m
N	39	128
d	$\lambda/2$	$\lambda/2$
v	100 m/s	100 m/s
f_{PR}	105.3 Hz	104.2 Hz
W_x	1 km	2 km
W_y	1 km	2 km

TABLE II: Simulation results for simulation # 1.

Algorithm	Rel. speed	Contrast	Max. residual [dB]	δy [m]
BP	1	259.7	$-\infty$	0.2437
FFBP 1	240	187.4	-11	0.2981
FFBP 2	68	226.7	-15	0.2923
RSA	6	205.8	-21	0.2750
RMA	740	169.1	-17	0.3100
CSA	8440	73.7	-7	0.4412

TABLE III: Simulation results for simulation # 2.

Algorithm	Rel. speed	Contrast	Max. residual [dB]	δy [m]
BP	1	499.2	$-\infty$	0.0930
FFBP 1	368	402.1	-15	0.0973
FFBP 2	96	443.0	-17	0.0947
RSA	5	452.8	-18	0.0940
RMA	1520	398.8	-14	0.0946
CSA	12732	272.5	-10	0.1124

be expressed in closed form, but the principle of stationary phase (PSP) can be used to derive the required expressions. The RDA and the RMA require an interpolation to take into account the x-dependence of the point target response. The chirp scaling algorithm (CSA) [6], [16], [17] requires only complex multiplications and Fourier transforms. It requires an analytic expression for the uncompressed linear frequency modulated signal in the (r, k_y) domain, which is again derived by using the PSP [16]. The following processing steps of the CSA rely on additional approximations, which are valid for small fractional bandwidths and integration angles [6], [14].

IV. NUMERICAL RESULTS

A. Simulation setup

We use a numerical example to perform a comparative study between the MSAR imaging algorithms analyzed in this paper. This demonstrates the computational cost and the achieved image quality of the proposed MSAR FFBP algorithms compared to conventional frequency domain algorithms. Two data sets using the signal model (1) and a point target model for g were simulated. The simulation parameters are listed in Table I. The range resolution is 0.15 m and the PRF has been chosen in such a way, that the resulting approximated monostatic phase center positions are uniformly sampled. This represents an ideal case for the frequency domain algorithms. The locations of the point scatterers can be seen from the reconstructed SAR image in Fig. 4 (a). The size of the image was set to 1 km in cross-range (W_y) and 1 km in range (W_x) in the first example. The image size in the second example was two times larger. The pixel spacing of the images was set to be half the theoretical spatial resolution.

B. Simulation results

The image quality was assessed using three different quality measures. The contrast of the image is defined as the ratio between the standard deviation and the mean of the image intensities. The residual images for each algorithm were calculated by coherently subtracting the back-projection (BP) image from them, and the maximum residual is the maximum intensity of the residual image. The cross-range resolution (3 dB width of the main lobe of the point target response) was calculated using four different point scatterers across the image and taking the mean of those values. These quality measures were chosen to take into account spatially variant defocusing effects such as phase and amplitude distortions. The results of this comparative study are shown in Tables II and III. The algorithms compared in this study are BP as the gold-standard reference, FFBP algorithms using the multispotlight technique (12) (FFBP 1) and the phase center approximation (9) (FFBP 2), RSA, RMA, and CSA.

In both examples, the FFBP algorithms were approximately two orders of magnitude faster than BP. The multispotlight technique (FFBP 1) was approximately four times faster than FFBP 2. However, it resulted in a lower image contrast and lower resolution than FFBP 2. Only RSA produced a better image quality than the FFBP algorithms in both experiments. This is significant, because the simulation setup represents an idealized case for the frequency domain algorithms. While CSA was the fastest algorithm, the approximations used in it broke down in these examples and resulted in the lowest image quality. RMA was an order of magnitude faster than any time domain algorithm, but it resulted in a lower contrast and lower cross-range resolution than RSA or the time domain algorithms. Although RSA produced better cross-range resolution and a smaller maximum residual than the FFBP algorithms, it was an order of magnitude slower.

V. DISCUSSION

The purpose of the simple numerical example was to compare the computational speed and accuracy of the MSAR algorithms. In this completely ideal situation, the FFBP algorithms were not much slower and produced a slightly better image quality than most of the frequency domain algorithms. The FFBP algorithms can be utilized for non-linear flight trajectories and non-uniform spatial sampling without significantly increasing the computational burden or reducing the image quality. The same does not hold true for the frequency domain algorithms, which require more complicated processing schemes to deal with non-ideal conditions.

The memory requirements are also of practical interest. As the image size becomes larger, the amount of available memory becomes a bottleneck for the FFT-based algorithms. However, the memory requirements of the FFBP algorithms
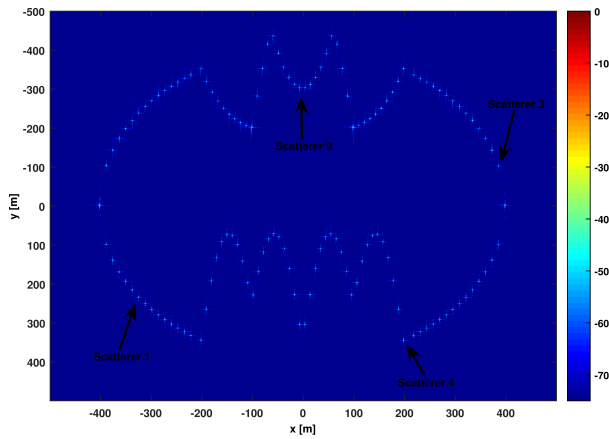
(a) Reconstructed SAR image using FFBP 2.
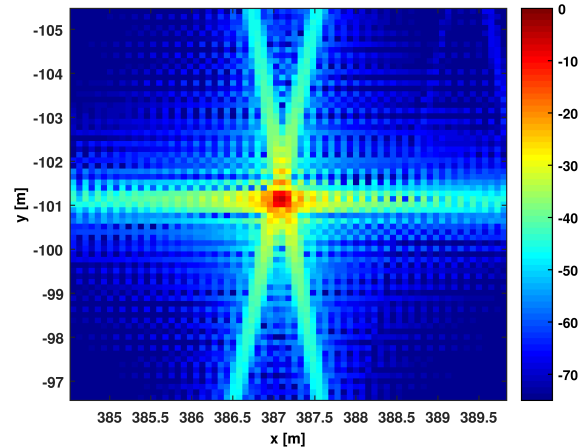
(b) Point target response (scatterer 3).

Fig. 4: The image quality was assessed by analyzing the contrast, the maximum residual value, and the cross-range resolution of the SAR image (a). The cross-range resolution was estimated as the mean of the 3 dB widths of the main lobes of four different point target responses (b) across the image.

can be adjusted. The images are reconstructed in a piecewise manner, which allows for a compromise between the required memory and computational speed. This provides yet another important advantage for time domain image reconstruction.

Time domain algorithms can be utilized for any type of trajectory or antenna array. They are also tractable for short-range and near-field imaging applications. Applications such as along-track interferometry benefit from fast and accurate image reconstruction, such as the proposed MSAR algorithms.

VI. CONCLUSION

In this paper, we analyzed an MSAR system, in which each receiver signal is independently quadrature demodulated and stored. We proposed fast time domain algorithms for MSAR based on digital beamforming, the phase center approximation, and the FFBP algorithm. Time domain algorithms significantly reduce the requirements for the imaging geometry and the sampling of the MSAR signal. Our comparative study showed that the proposed algorithms are computationally feasible and advantageous for MSAR imaging. The flexibility provided by the combination of a multichannel system and time domain image reconstruction can be used to significantly increase the performance of SAR systems.

ACKNOWLEDGEMENT

REFERENCES

[1] D. Cerutti-Maori and I. Sikaneta, "A generalization of DPCA processing for multichannel SAR/GMTI radars," *IEEE Transactions on Geoscience and Remote Sensing*, vol. 51, no. 1, pp. 560–572, Jan. 2013.

[2] P. A. Rosen, S. Hensley, R. I. Joughin, F. K. Li, S. N. Madsen, E. Rodriguez, and R. M. Goldstein, "Synthetic aperture radar interferometry," *Proceedings of the IEEE*, vol. 88, no. 3, pp. 333–381, Mar. 2000.

[3] N. Gebert, G. Krieger, and A. Moreira, "Digital beamforming on receive: Techniques and optimization strategies for high resolution wide-swath SAR imaging," *IEEE Transactions on Aerospace and Electronic Systems*, vol. 45, no. 2, pp. 564–592, Apr. 2009.

[4] M. Younis, C. Fischer, and W. Wiesbeck, "Digital beamforming in SAR systems," *IEEE Transactions on Geoscience and Remote Sensing*, vol. 41, no. 71, pp. 1735–1739, Jul. 2003.

[5] R. Bamler, "A comparison of range-Doppler and wavenumber domain SAR focusing algorithms," *IEEE Transactions on Geoscience and Remote Sensing*, vol. 30, no. 4, pp. 706–713, Jul. 1992.

[6] R. K. Raney, H. Runge, R. Bamler, I. G. Cumming, and F. H. Wong, "Precision SAR processing using chirp scaling," *IEEE Transactions on Geoscience and Remote Sensing*, vol. 32, no. 4, pp. 786–799, Jul. 1994.

[7] C. Cafforio, C. Prati, and F. Rocca, "SAR data focusing using seismic migration techniques," *IEEE Transactions on Aerospace and Electronic Systems*, vol. 27, no. 2, pp. 194–207, Mar. 1991.

[8] D. C. Munson, J. D. O'Brien, and W. K. Jenkins, "A tomographic formulation of spotlight-mode synthetic aperture radar," *Proceedings of the IEEE*, vol. 72, no. 8, pp. 917–925, Aug. 1983.

[9] M. Soumekh, *Synthetic Aperture Radar Signal Processing with MATLAB Algorithms*. New York: Wiley, 1999.

[10] J. Jylhä, M. Väilä, H. Perälä, V. Väisänen, R. Vehmas, J. Kylmälä, V.-J. Salminen, and A. Visa, "On SAR processing using pixel-wise matched kernels," in *Proceedings of the 11th European Radar Conference (EuRAD 2014)*, Oct. 2014, pp. 97–100.

[11] A. F. Yegulalp, "Fast backprojection algorithm for synthetic aperture radar," in *Proceedings of the 1999 IEEE Radar Conference*, Apr. 1999, pp. 60–65.

[12] L. M. H. Ulander, H. Hellsten, and G. Stenström, "Synthetic-aperture radar processing using fast factorized back-projection," *IEEE Transactions on Aerospace and Electronic Systems*, vol. 39, no. 3, pp. 760–776, Jul. 2003.

[13] J. C. Curlander and R. N. McDonough, *Synthetic Aperture Radar: Systems and Signal Processing*. New York: Wiley, 1991.

[14] W. G. Carrara, R. S. Goodman, and R. M. Majewski, *Spotlight Synthetic Aperture Radar: Signal Processing Algorithms*. Boston, MA: Artech House, 1995.

[15] F. Rocca, C. Cafforio, and C. Prati, "Synthetic aperture radar: A new application for wave equation techniques," *Geophysical Prospecting*, vol. 37, no. 7, pp. 809–830, Oct. 1989.

[16] R. K. Raney, "A new and fundamental Fourier transform pair," in *Proceedings of IEEE International Geoscience and Remote Sensing Symposium (IGARSS)*, May 1992, pp. 106–107.

[17] A. Moreira, J. Mittermayer, and R. Scheiber, "Extended chirp scaling algorithm for air- and spaceborne SAR data processing in stripmap and ScanSAR imaging modes," *IEEE Transactions on Geoscience and Remote Sensing*, vol. 34, no. 5, pp. 1123–1136, Sep. 1996.